



Contents lists available at ScienceDirect

Journal of Sound and Vibration

journal homepage: www.elsevier.com/locate/jsv

Enhancing wave retarding and sound absorption performances in perforation-modulated sonic black hole structures

Sihui Li, Xiang Yu^{*}, Li Cheng^{*}

Department of Mechanical Engineering, The Hong Kong Polytechnic University, Kowloon, Hong Kong, China

ARTICLE INFO

Keywords:

Perforation-modulated sonic black hole
Perforation parameters
Wentzel-Kramers-Brillouin method
Slow wave absorber

ABSTRACT

Sonic black hole (SBH) effects in a retarding duct can be exploited for sound wave manipulation and absorption. The phenomenon relies on two fundamental physical mechanisms: wave speed reduction and energy dissipation. In this study, we demonstrate that these two physical processes can be meticulously balanced through adjusting the perforation parameters in a perforation-modulated SBH (PMSBH). To elucidate the mechanism of slow wave generation and the effect of perforation parameters, an analytic model based on the Wentzel-Kramers-Brillouin (WKB) solutions to the linear acoustic wave equation is established. Alongside transient finite element simulations, the study unveils the roles that major physical parameters play in terms of regulating sound speed and sound absorption. The perforation ratio of the PMSBH is identified as the dominant factor affecting the slow-sound effect, with an optimal range of above 10 % for a PMSBH with densely segmented internal rings. Owing to the inclusion of the perforated boundary, prominent slow wave effects can still be maintained even with a reduced number of rings, provided that the perforation ratio is properly chosen within a reduced variation range. In both cases, the identified perforation ratio largely exceeds the conventional range widely adopted in the micro-perforation community when the slow wave effects are absent. On top of this, tuning the hole size can further enhance air friction for better sound absorption. Theoretical and numerical findings are experimentally validated, and the performance of the PMSBH is demonstrated. While bringing forward the concept of tunable design, this study offers physical insights and guidance for realizing effective sound absorbers embracing slow wave principles and perforation-induced sound absorption.

1. Introduction

The realization of various acoustic functions through the manipulation of sound waves has long been an area of great interest to the acoustics community. Structural acoustic black hole (ABH), as a means of manipulating flexural waves in beams or plates, has gained significant research attention in recent years [1–7]. In a one-dimensional ABH, for example, the thickness of the structure gradually decreases according to a power law [8,9]. As flexural waves propagate towards the wedge-shaped termination, the velocity progressively decreases, before being trapped and absorbed at the tip end, albeit the existence of unavoidable residual truncation thickness [10]. The phenomenon, referred to as slow wave effect, exhibits several salient features like wavelength compression and energy accumulation, which are essential for effective energy dissipation [11–13]. Research on ABHs has been increasing rapidly in

^{*} Corresponding authors.

E-mail addresses: lucien.yu@polyu.edu.hk (X. Yu), li.cheng@polyu.edu.hk (L. Cheng).

<https://doi.org/10.1016/j.jsv.2024.118765>

Received 3 June 2024; Received in revised form 15 August 2024; Accepted 7 October 2024

Available online 9 October 2024

0022-460X/© 2024 Elsevier Ltd. All rights are reserved, including those for text and data mining, AI training, and similar technologies.

recent years, covering various aspects such as effective modeling methods [14,15], basic ABH structural designs [16–20], periodic structures, complex functional structures [21–25], etc. The research on ABH provides new opportunities for technological breakthroughs in vibration control, noise reduction, energy harvesting, and many other applications.

Sonic black hole (SBH), as the counterpart of the structural ABH, also holds great promise in manipulating and absorbing sound waves in air [26–29]. SBH is typically constructed inside an acoustic duct with a decreasing cross-sectional area formed by a large number of rings (infinite in theory) with gradually reducing inner radius. Similar to ABH, SBH exhibits the slow wave effect owing to a gradually varying acoustic admittance produced by the rings. In the ideal scenario, the sound speed can be reduced to zero at the duct termination, leading to accumulated sound energy and minimal sound reflection with proper absorption treatment. The pioneering work by Mironov provided the first theoretical framework and proof of the slow wave effect [30]. Subsequently, numerical and theoretical methods have been developed to study the acoustic performance and underlying physical mechanisms of SBH structures [31–34]. The influence of various parameters has also been investigated, laying the foundations for subsequent engineering design and applications [35–38]. Furthermore, several studies have proposed different types of SBH structures inspired by the original SBH design [39], such as the external SBH muffler [40,41], lattice absorbers with SBH [42] and periodic SBH structures [43]. Recently, some preliminary studies on SBH with rectangular cross-section have also been initiated [44,45]. Meanwhile, experimental progress has demonstrated effective sound absorption and slow wave effects in SBH structures [46]. Despite these efforts [29,47–49], SBH has received less attention compared to structural ABH, which warrants more concerted research efforts to explore the physical mechanisms and potential applications of the SBH.

Our recent work proposed a novel SBH-inspired retarding structure, which incorporates a perforated liner to enhance the SBH performance [50]. While the use of the perforated boundary was shown to promote sound absorption and slow wave effect as compared to the original SBH, the underlying mechanism and design flexibility offered by the perforated boundary were not fully explored. In addition, numerous parameters involved in the system make it extremely challenging to achieve an optimal design without theoretical tools and guidance. This adds to the lack of understanding of the roles they play in terms of affecting slow wave phenomena and sound absorption. These research gaps motivate the present study.

More specifically, this study aims to advance the predictive theory on SBH and elaborate on the tuning ability of the perforation-modulated boundary (PB) to enhance the black hole effects and ultimately SBH-enabled sound absorption. The structure under investigation, referred to as the perforation-modulated SBH (PMSBH), is shown in Fig. 1. It comprises two essential components, the original SBH configuration [30], consisting of a series of rings with gradually decaying inner radius, and the perforation-modulated boundary, whose parameters can be adjusted in a wide range. The introduction of the perforation-modulated boundary allows for tunability within the SBH structure so that the slow wave phenomenon and sound absorption can be tuned and properly balanced

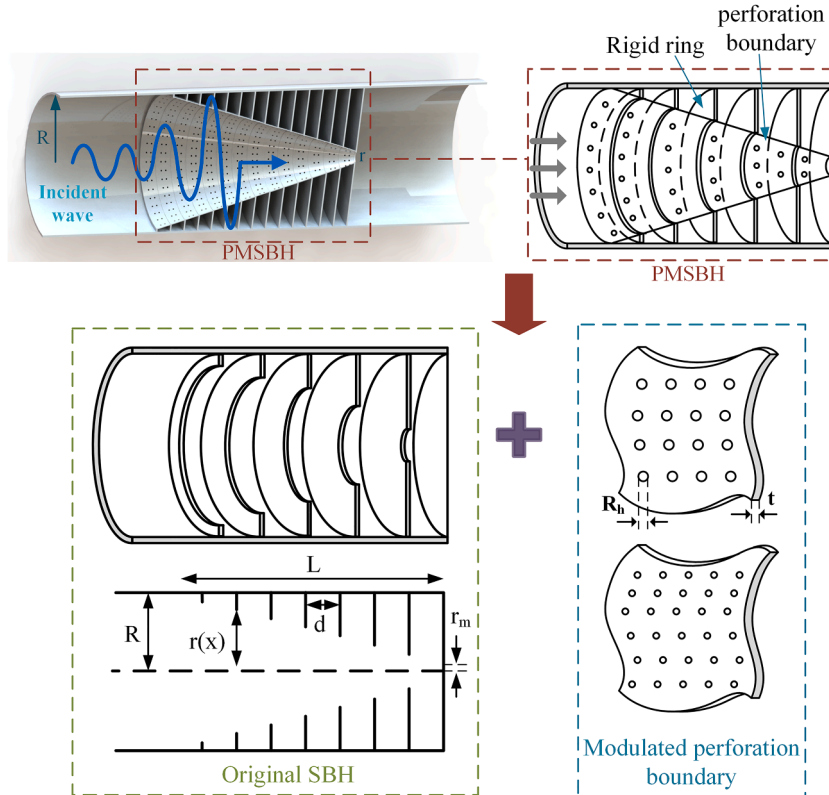


Fig. 1. Overall structure of the proposed PMSBH model.

through perforation modulation. This study has three primary objectives thus showing its novelty: First, we establish an analytical method to predict the wave speed variation inside the PMSBH structure, thus extending the pioneering Mironov's model to include the perforated boundary effects. Second, through mechanism exploration, we seek ways to tune the interplay between the slow wave effect and sound absorption in the PMSBH. Third, we report experimental results to validate the predictive model and verify numerically predicted results. The study aims to establish a set of criteria for modulating the PMSBH, which can guide future designs of sound absorbers and other related devices based on SBH principles.

The rest of the paper is organized as follows. Section 2 first derives the Wentzel-Kramers-Brillouin (WKB) solutions for the PMSBH in two different cases, where both continuous and discrete admittance variations are considered. The range of applicability of the analytical solution is analyzed in Section 3. Section 4 validates the accuracy of the WKB solution and then investigates the influence of perforation parameters and the number of rings on the slow wave effect and sound absorption, using both WKB and FEM approaches. The section summarizes the criteria for tuning the perforation boundary to enhance the black hole effects. Experimental validations are given in Section 5 before concluding the paper.

2. Theory

We investigate a PMSBH structure with variable perforation parameters. We first develop WKB solutions for the PMSBH, considering two different configurations: continuous and discrete admittance variation.

2.1. Formulation of the PMSBH

We first derive the governing equations for the PMSBH model. Fig. 2 provides a schematic representation of the structure, for which two different approaches are taken for modeling the PMSBH depending on the number of rings involved. For a PMSBH with a sufficiently large number of rings (depicted in the left figure of Fig. 2), the admittance at the PB is treated as continuous. Otherwise, the right figure illustrates the case where the PMSBH has a small number of rings, thus requiring the admittance at the PB to be treated as discrete. In both cases, the x -axis is selected as the symmetric axis in the waveguide. By defining an infinitesimal layer of air element of thickness dx , the linear Euler equation writes [30]:

$$-\frac{\partial p}{\partial x} = \rho_0 \frac{\partial v}{\partial t}, \quad (1)$$

where p is the sound pressure; ρ_0 the air density; v the acoustic particle velocity. According to the law of conservation of matter, air enters this thin layer from the left side and upper cavity and exits from the right side, yielding the equation of continuity:

$$d(\rho_0 S v) + (2\pi r v_+ \rho_0) dx + \frac{\partial p}{\partial t} S dx = 0, \quad (2)$$

where S is the cross-sectional area of the thin layer; r the inner radius; v_+ the projection of the particle velocity at the PB along the

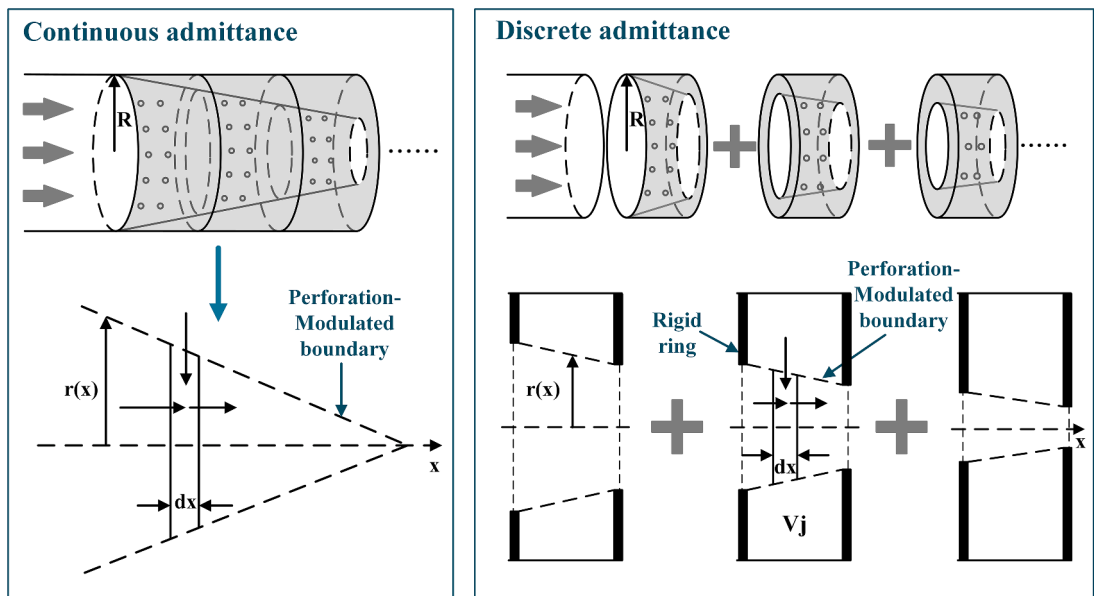


Fig. 2. Wall admittance treatment of the PMSBH structure. Left: continuously varying admittance with a large number of rings; Right: discretely varying admittance with a small number of rings.

direction perpendicular to the symmetry axis. Note that the relationship between the velocity v_+ and the pressure p is easily obtained as $v_+ = Yp$ based on the definition of acoustic admittance, where Y represents the acoustic admittance at the PB. This formula can be substituted into Eq. (2). Meanwhile, the equation of state should be satisfied in this thin layer, yielding

$$\frac{\partial \rho}{\partial t} = \frac{1}{c^2} \frac{\partial p}{\partial t}, \quad (3)$$

where c is the speed of sound in air. Then, by Eqs. (1)–(3), we can obtain the wave equation in terms of acoustic pressure,

$$\frac{1}{c^2} \frac{\partial^2 p}{\partial t^2} + \frac{2Y\rho_0}{r} \frac{\partial p}{\partial t} = \frac{\partial^2 p}{\partial x^2} + \frac{\partial p}{\partial x} (\ln S)'_x. \quad (4)$$

Subsequently, for time-harmonically varying pressures, Eq. (4) can be transformed into the generalized Webster equation,

$$p'' + p' (\ln S)' + p \left(k_0^2 + \frac{2Y\rho_0}{r} (i\omega) \right) = 0, \quad (5)$$

where k_0 is the wave number in air and i the imaginary unit. Eq. (5) needs to be solved to get the analytical solution of the PMSBH model. The calculation of the admittance at the PB Y in the structure is of great importance in this analysis. Depending on whether the admittance Y should be considered continuous or discrete, we can proceed to solve the wave equation and obtain the corresponding solutions in two different cases, to be detailed hereafter.

2.2. WKB solution through continuous admittance treatment

When the PMSBH has a large number of rings, meaning the distance between two adjacent rings is sufficiently small, the admittance at PB can be treated as continuously varying along x direction, as shown in the left schematic of Fig. 2. In this situation, the surface impedance at PB can be expressed as Eq. (6), combining the impedance of the perforation-modulated boundary with that of the backing air cavity:

$$Z_{total} = \frac{2\rho_0 c^2 r}{(-i\omega)(R^2 - r^2)} - \left(\frac{4h}{R_h} + 4 \right) \frac{R_s}{\varphi} - i \frac{\omega \rho_0}{\varphi} (2\varepsilon_e + h) - i \left(\frac{4h}{R_h} + 4 \right) \frac{R_s}{\varphi}, \quad (6)$$

$$R_s = \frac{1}{2} \sqrt{2\eta\omega\rho_0}. \quad (7)$$

$$\varepsilon_e = 0.48 \sqrt{\pi \left(\frac{R_h}{2} \right)^2} \left(1 - 1.47 \sqrt{\varphi} + 0.47 \sqrt{\varphi^3} \right), \quad (8)$$

where ω is the angular velocity; R the radius of the duct; h the thickness of the PB; R_h the orifice diameter of the PB; φ the perforated ratio of the PB; R_s the surface resistance and η the dynamic viscosity of air. ε_e represents a correction length. The first term in Eq. (6) represents the impedance of the back cavity, which is a continuously varying function because of the gradual change in the depth of the cavity behind the perforated boundary. The remaining terms are related to the perforation boundary. Here, Beranek Ingard's model is selected to calculate the impedance of the PB. The real part of the chosen formula is the acoustic resistance, which is correlated with the dissipation of sound energy due to viscous effects. The imaginary part, which is the acoustic reactance, represents the inertial effects. The reasons and benefits of choosing this modeling method for the PB have been presented and validated in our previous work [50] and are omitted here. By grouping the parameters in Eq. (6), the total surface impedance of the perforated boundary writes:

$$Z_{total} = A + iB, \quad (9)$$

$$A = - \left(\frac{4h}{R_h} + 4 \right) \frac{R_s}{\varphi}, \quad (10)$$

$$B = \frac{2\rho_0 c^2 r}{\omega(R^2 - r^2)} - \frac{\omega \rho_0}{\varphi} (2\varepsilon_e + h) - \left(\frac{4h}{R_h} + 4 \right) \frac{R_s}{\varphi}. \quad (11)$$

The admittance Y at the PB can be obtained as $Y = 1/Z_{total} = 1/(A + iB)$. Substituting Y and $S = \pi r^2$ into Eq. (5) gives:

$$p'' + 2p' (\ln r)' + p \left(k_0^2 + \frac{2\rho_0 \omega}{r(B - iA)} \right) = 0. \quad (12)$$

The WKB method can be applied to solve Eq. (12) for acquiring an approximate solution. It is important to note that the utilization of the WKB method requires certain conditions, which will be discussed in detail in later sections. First, assuming the applicability of the WKB method is satisfied, we assume $p(x) \sim \exp(ikx)$ and substitute it in Eq. (12). Then Eq. (12) can be replaced by the following equation in terms of the local wave number k in the PMSBH,

$$-k^2 + 2ik(\ln r)' + \left(k_0^2 + \frac{2\rho_0\omega}{r(B-iA)}\right) = 0. \quad (13)$$

Solving Eq.(13) yields the local wave number $k(x)$ as,

$$k(x) = \sqrt{\left(k_0^2 + \frac{2\rho_0\omega}{r(B-iA)}\right) - ((\ln r)')^2}. \quad (14)$$

The inner radius of the PMSBH can decrease according to different power laws. Hereafter, we take the basic case in which the PMSBH is assumed to be a linear acoustic black hole structure, *i.e.*, the inner radius of the ring linearly reduces to 0, following $r = -Rx/L$, where L is the length of the PMSBH. In this case, the local wave number for the ideal linear PMSBH can be obtained from Eq. (14) and expressed as,

$$k(x) = \sqrt{k_0^2 + \frac{2\rho_0\omega L}{Rx\left(-\left(\frac{4h}{R_h} + 4\right)\frac{R_s}{\varphi}i + \frac{2\rho_0c^2RLx}{\omega(R^2L^2 - R^2x^2)} + \frac{\omega\rho_0}{\varphi}(2\varepsilon_e + h) + \left(\frac{4h}{R_h} + 4\right)\frac{R_s}{\varphi}\right) - \frac{1}{x^2}}. \quad (15)$$

The corresponding phase velocity and the group velocity can be obtained according to their respective definitions, writing

$$c_p = \frac{\omega}{k} = \frac{\omega}{\sqrt{k_0^2 + \frac{2\rho_0\omega L}{Rx\left(-\left(\frac{4h}{R_h} + 4\right)\frac{R_s}{\varphi}i + \frac{2\rho_0c^2RLx}{\omega(R^2L^2 - R^2x^2)} + \frac{\omega\rho_0}{\varphi}(2\varepsilon_e + h) + \left(\frac{4h}{R_h} + 4\right)\frac{R_s}{\varphi}\right) - \frac{1}{x^2}}}, \quad (16)$$

$$c_g = \frac{d\omega}{dk} = \left(\frac{dk}{d\omega}\right)^{-1}. \quad (17)$$

Once the group velocity in the PMSBH is obtained, the time taken for the sound wave to travel and reach different positions inside the PMSBH can be determined, which is conducive to the investigation of the slow wave phenomena, to be demonstrated in later sections.

2.3. WKB solution through discrete admittance treatment

When the number of rings in the PMSBH is small, the assumptions made in the previous case are no longer valid. The increased distance between the rings necessitates treating the air cavity enclosed by the rings and the PB as a separate volume, resulting in discontinuities in the admittance between the air cavities. In this case, we discretize it and consider the region between the two rings as an individual unit. For a unit j , we extract and analyze a thin layer of thickness dx at the inner region. Although the unit follows the same wave equation as Eq. (5), the calculation of Y is different from that in Section 2.2, specifically the treatment of the backing air cavity. While still using Beranek Ingard's model to calculate the PB's impedance, the air cavity is treated as a lumped volume to get the total acoustic impedance [50]. The average value, which is the surface impedance of the contact surface between the cavity and the PB, can be acquired by dividing the lumped volume in the total acoustic impedance by the PB area. This yields

$$Z_{total-j} = i\frac{Z_0S_j}{k_0V_j} - \left(\frac{4h}{R_h} + 4\right)\frac{R_s}{\varphi} - i\frac{\omega\rho_0}{\varphi}(2\varepsilon_e + h) - i\left(\frac{4h}{R_h} + 4\right)\frac{R_s}{\varphi}, \quad (18)$$

where Z_0 is the characteristic impedance of air; S_j the area of the PB in the unit j and V_j the volume of the air cavity. Similarly, the first term in the $Z_{total-j}$ expression represents the air cavity, and the other three terms are the impedance of the PB. Then Eq. (18) can also be simplified as,

$$Z_{total-j} = A_j + iB_j, \quad (19)$$

$$A_j = -\left(\frac{4h}{R_h} + 4\right)\frac{R_s}{\varphi}, \quad (20)$$

$$B_j = \frac{Z_0S_j}{k_0V_j} - \frac{\omega\rho_0}{\varphi}(2\varepsilon_e + h) - \left(\frac{4h}{R_h} + 4\right)\frac{R_s}{\varphi}. \quad (21)$$

Likewise, the admittance $Y_j = 1/Z_{total-j} = 1/(A_j + iB_j)$. Substituting Y_j into Eq. (5), we can obtain the transformed wave equation similar to Eq. (12) as,

$$p'' + 2p'(\ln r)' + p\left(k_0^2 + \frac{2\rho_0\omega}{r(B_j - iA_j)}\right) = 0. \quad (22)$$

Similarly, we use the WKB approximate to solve Eq. (22), which gives the local wave number $k_j(x)$ in the unit j , expressed as

$$k_j = \sqrt{\left(k_0^2 + \frac{2\rho_0\omega}{r(B_j - iA_j)}\right) - ((\ln r)')^2}. \tag{23}$$

For the same linear PMSBH,

$$k_j = \sqrt{k_0^2 + \frac{2\rho_0\omega L}{Rx\left(-\left(\frac{4h}{R_h} + 4\right)\frac{R_s}{\varphi}i - \frac{Z_0S_j}{k_0V_j} + \frac{\omega\rho_0}{\varphi}(2\mathcal{E}_e + h) + \left(\frac{4h}{R_h} + 4\right)\frac{R_s}{\varphi}\right) - \frac{1}{x^2}}. \tag{24}$$

After acquiring the local wave number in each unit, the phase velocity and the group velocity can be determined via Eqs. (16) and (17). This solution will be used to investigate the physical properties of the PMSBH with a reduced ring number. In passing, the method can also be used to model other complex structures, such as the PMSBH with different PBs in each unit.

2.4. Applicability conditions of the WKB solutions

The validity of the WKB solution for the PMSBH relies on the applicability of the WKB method, which is subject to certain conditions that need to be satisfied. In this section, we outline the range of applicability of the WKB method for the PMSBH with continuous admittance. Specifically, the WKB approximation is applicable if the coefficient in Eq. (12) only exhibits slight variations within the wavelength range. Consequently, this leads to the following two inequalities,

$$\left|\frac{d(\ln r)'}{dx} \frac{1}{k}\right| < |(\ln r)'|, \tag{25}$$

$$\left|\frac{d\left(\frac{1}{r(B-iA)}\right)}{dx} \frac{1}{k}\right| < \left|\frac{1}{r(B-iA)}\right|. \tag{26}$$

From these two inequalities, it follows that

$$|k| > \left|\frac{r''}{r'} - \frac{r'}{r}\right|, \tag{27}$$

$$|k| > \left|\frac{r'}{r} + \frac{(B-iA)'}{(B-iA)}\right|. \tag{28}$$

Defining two new parameters, C_1 and C_2 , one has

$$C_1 = |k| - \left|\frac{r''}{r'} - \frac{r'}{r}\right| > 0, \tag{29}$$

$$C_2 = |k| - \left|\frac{r'}{r} + \frac{(B-iA)'}{(B-iA)}\right| > 0. \tag{30}$$

Therefore, when using the WKB solutions, C_1 and C_2 have to be positively valued at each position in the PMSBH structure. Similarly, if the PMSBH is a linear structure and the inner radius varies according to $r = -Rx/L$, one has

$$C_1 = |k| - \left|\frac{1}{x}\right| > 0, \tag{31}$$

$$C_2 = \left| |k| - \frac{1}{x} - \frac{\frac{2\rho_0c^2L(L^2+x^2)}{R\omega(L^2-x^2)^2}}{\left(\frac{4h}{R_h} + 4\right)\frac{R_s}{\varphi}i - \frac{2\rho_0c^2RLx}{\omega(R^2L^2-R^2x^2)} - \frac{\omega\rho_0}{\varphi}(2\mathcal{E}_e + h) - \left(\frac{4h}{R_h} + 4\right)\frac{R_s}{\varphi}} \right| > 0. \tag{32}$$

The calculated values of C_1 and C_2 defined above will be used to ensure the validity of the WKB solutions.

3. Validation and applicability of the WKB solution

As a start, this section validates the accuracy and applicability of the WKB method derived in this work. First, the validity of the WKB solution is assessed through comparisons with numerical simulations. Following that, the applicable range for the proposed PMSBH structure is determined by investigating the influence of various parameters on the accuracy of the WKB solution.

3.1. Validation of the WKB approximation

The proposed WKB method is first assessed. In this part, within the applicable range of the WKB method, the accuracy of the WKB solutions for the PMSBH with continuous or discrete admittance treatment is verified through two different approaches: comparison with Mironov's model and with the finite element method (FEM). Thus, this section is divided into two parts to address each approach separately.

3.1.1. Comparison with Mironov's model

We first present a comparison between the results obtained from the WKB model and those from the Mironov's model [30] in the special case of a bare SBH structure consisting of rings only without perforated boundary. Meanwhile, the WKB solution is used to theoretically demonstrate the existence of the slow wave effect. In the present WKB solution, the perforation ratio φ is set to 1. The parameters of the linear SBH used are tabulated in Table 1, in which r_m is the minimum inner radius of the rings at the SBH truncation; N the number of rings and d the distance between two adjacent rings. Other physical quantities used in the calculation are: $\eta = 1.86 \times 10^{-5}$ Pa·s, $\rho_0 = 1.215$ kg/m³ and $c_0 = 340$ m/s.

The variation of the sound wave velocity in the SBH structure at 1000 Hz is shown in Fig. 3, in which the present WKB solutions and Mironov's original solutions are compared, with Fig. 3(a) and (b) corresponding to continuous and discrete impedance models in WKB solutions. As observed in both figures, the derived WKB solutions agree well with the benchmark solutions. Before entering the SBH section, the sound wave propagates at a uniform speed of 340 m/s before gradually slowing down as it enters the SBH. Since the selected SBH has a truncated end and its termination radius does not perfectly decrease to zero, the velocity does not reduce to zero either.

3.1.2. Validation against FEM results

To further verify the accuracy of the derived WKB solutions for the PMSBH, FEM results are employed as a reference. For FEM, the PMSBH is modeled using transient simulation in COMSOL Multiphysics to calculate the sound velocity changes as the wave packet propagates through the structure. The schematic of the PMSBH model is shown in Fig. 4. An incident plane wave is defined at the entrance of the duct, which is filled with air with $\rho_0 = 1.215$ kg/m³ and $c_0 = 340$ m/s. The damping loss in the PMSBH region is considered by using a complex sound speed $c_0 = 340 \times (1 + 0.01i)$ m/s. The "Interior Impedance" option in Comsol is applied to model the PB attached to the SBH, with its impedance calculated using Beranek Ingard's model [50]. The PMSBH has the same truncation at the end as the one used above. To accurately detect the wavefront of the sound wave propagation in transient analysis, the reflection of the sound wave should be eliminated as much as possible, which is achieved by connecting a duct extension of the same radius to the outlet. Additionally, a perfectly matched layer is placed at the end of this elongated duct to eliminate reflections. The length of this prolonged tube is 450 mm. The parameters of the PMSBH configuration are given in Table 2.

The sound velocity variations calculated by FEM are plotted in Fig. 5. Through transient simulations, the relationship between position and time of wave propagation in the PMSBH structure can be obtained. A smoothly fitted curve further allows us to calculate the local velocity at each point by determining the slope of the curve. The fitting method employed was polynomial fitting up to the fourth order. The derived WKB approximated solution to the same PMSBH structure is then applied to obtain the velocity profile. The results of the WKB solution for the continuous impedance model and the discrete impedance model are presented in Fig. 5(a) and Fig. 5(b), respectively. From these two figures, it can be observed that the results obtained using the WKB method and FEM are in good agreement, with slight differences at the termination of the PMSBH when position x approaches 0. These minor differences can be attributed to the presence of reflected sound waves in the system, which makes the precise extraction of the arrival waves more difficult in FEM simulations. Nonetheless, the overall agreement between the WKB method and FEM confirms the accuracy of the WKB solution in predicting sound wave propagation inside the PMSBH structure. Furthermore, it is evident that the speed of the sound wave progressively decreases as it propagates through the PMSBH structure, indicating the occurrence of the slow wave phenomenon.

3.2. Applicable range of the WKB solutions

As discussed earlier, the WKB solution is limited to a specific range of applicability. This is further elaborated here to guide the implementation of the WKB solutions.

Adopting the definition of C_1 and C_2 in Eqs. (31) and (32), their values are calculated for various PMSBH configurations with results shown in Fig. 6. These configurations involve different perforation ratios φ and hole diameters R_h , covering a wide variation range for these parameters. Specifically, the chosen range for φ is from 0.005 to 0.6, and that of R_h between 0.2 mm and 4 mm, covering both micro- and macro- (typically larger than 1 mm) perforation cases. The remaining parameters are kept the same as those in Table 2, and the admittance of these models is treated as continuous. A representative frequency of 1000 Hz is chosen for the analysis.

In Fig. 6, the purple area indicates the range of perforation parameters that satisfy condition 1 ($C_1 > 0$). It can be observed that

Table 1
Parameters for the selected SBH.

| | $R(\text{mm})$ | $r_m(\text{mm})$ | $L(\text{mm})$ | N | $d(\text{mm})$ |
|-----|----------------|------------------|----------------|-----|----------------|
| SBH | 48 | 3 | 150 | 39 | 3.75 |

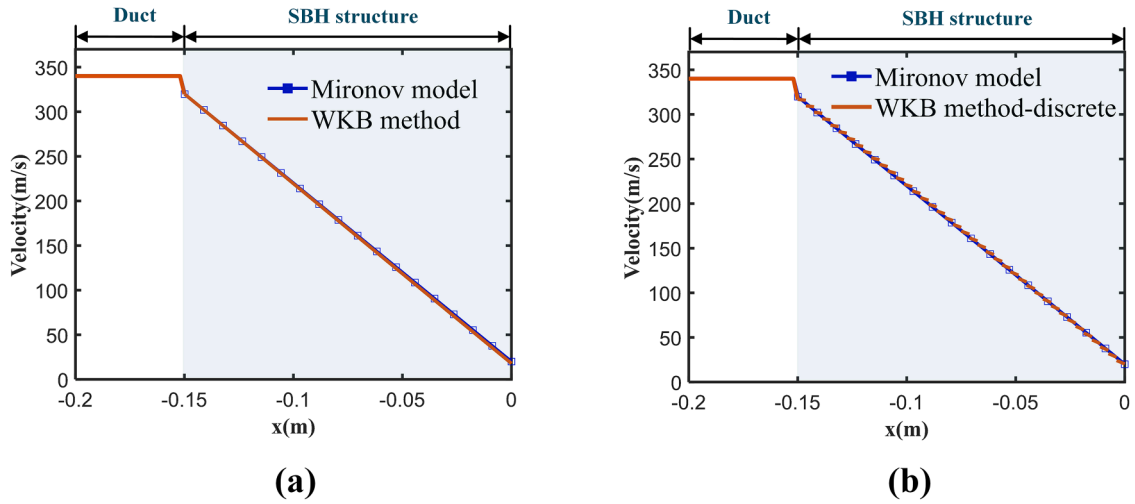


Fig. 3. Comparison of sound velocity in the SBH structure. (a) WKB solution with continuous admittance treatment against Mironov's model (b) WKB solution with discrete admittance treatment against Mironov's model.

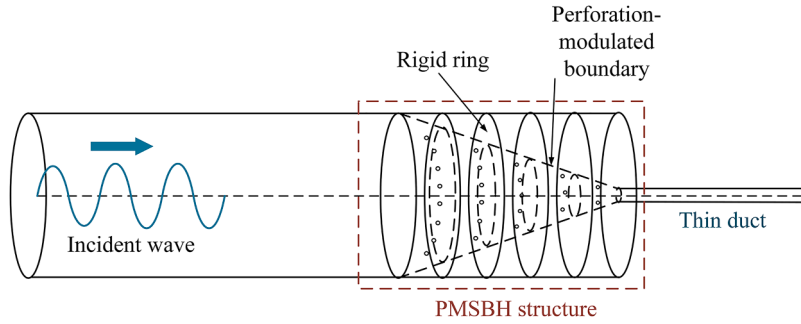


Fig. 4. Schematic of the PMSBH model in COMSOL.

Table 2

Parameters for the determined PMSBH.

| | $R(\text{mm})$ | $r_m(\text{mm})$ | $L(\text{mm})$ | N | $d(\text{mm})$ | $h(\text{mm})$ | φ | $R_h(\text{mm})$ |
|-------|----------------|------------------|----------------|-----|----------------|----------------|-----------|------------------|
| PMSBH | 48 | 3 | 150 | 39 | 3.75 | 0.4 | 0.2 | 1 |

essentially all configurations fulfill this condition within the parameter variation range considered here, except for some cases with a small φ and a large R_h . The orange area indicates the range of parameters that satisfy condition 2 ($C_2 > 0$), which is smaller than that for condition 1. The overlapped area obviously pinpoints the valid parameter range where the WKB method can be applied. To illustrate this, two typical cases are chosen, one from the overlapped area with a φ of 0.4 and a R_h of 2 mm, satisfying both conditions; whilst the other one has a φ of 0.07 and a R_h of 2 mm from the purple section, which only satisfies condition 1. The values of C_1 and C_2 along the x positions for these two configurations are also presented in Fig. 6. It is evident that for the second case, C_2 is way below the zero line at around $x = -0.02$ m, indicating that the associated perforation parameters in the second case do not satisfy condition 2. Consequently, the WKB solution cannot be applied to this particular configuration.

4. Modulating PMSBH through perforated boundaries

In this section, we investigate the modulation mechanism of the PMSBH and propose design guidelines to maximize the wave retarding effect and sound absorption of the structure. Influences of various parameters on the slow wave effect as well as the sound absorption effect are first investigated. The possibility of using a reduced number of rings to simplify the structural design and materialization without compromising the SBH effects is also elucidated.

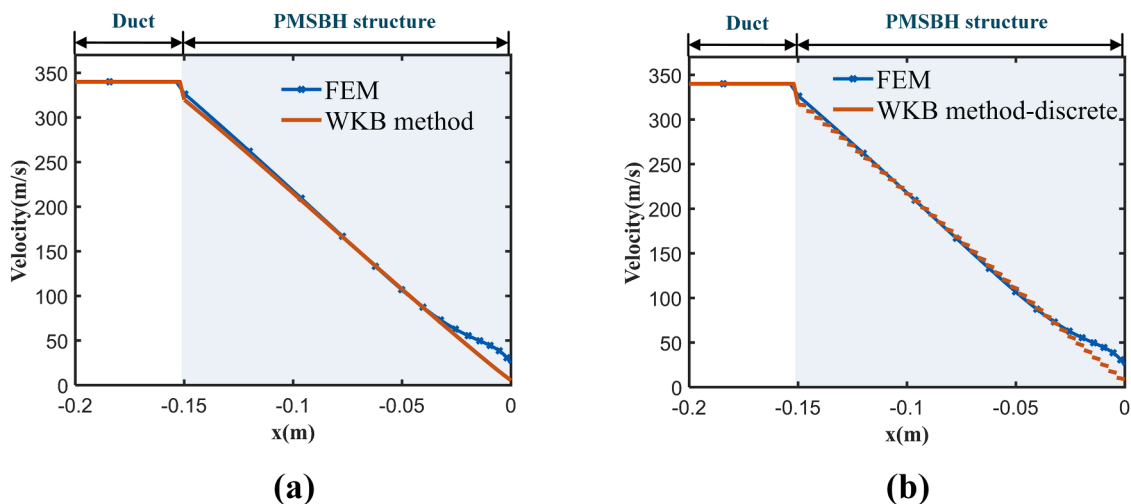


Fig. 5. Comparison of sound velocity in the PMSBH structure. (a) WKB solution with continuous admittance treatment against FEM results (b) WKB solution with discrete admittance treatment against FEM results.

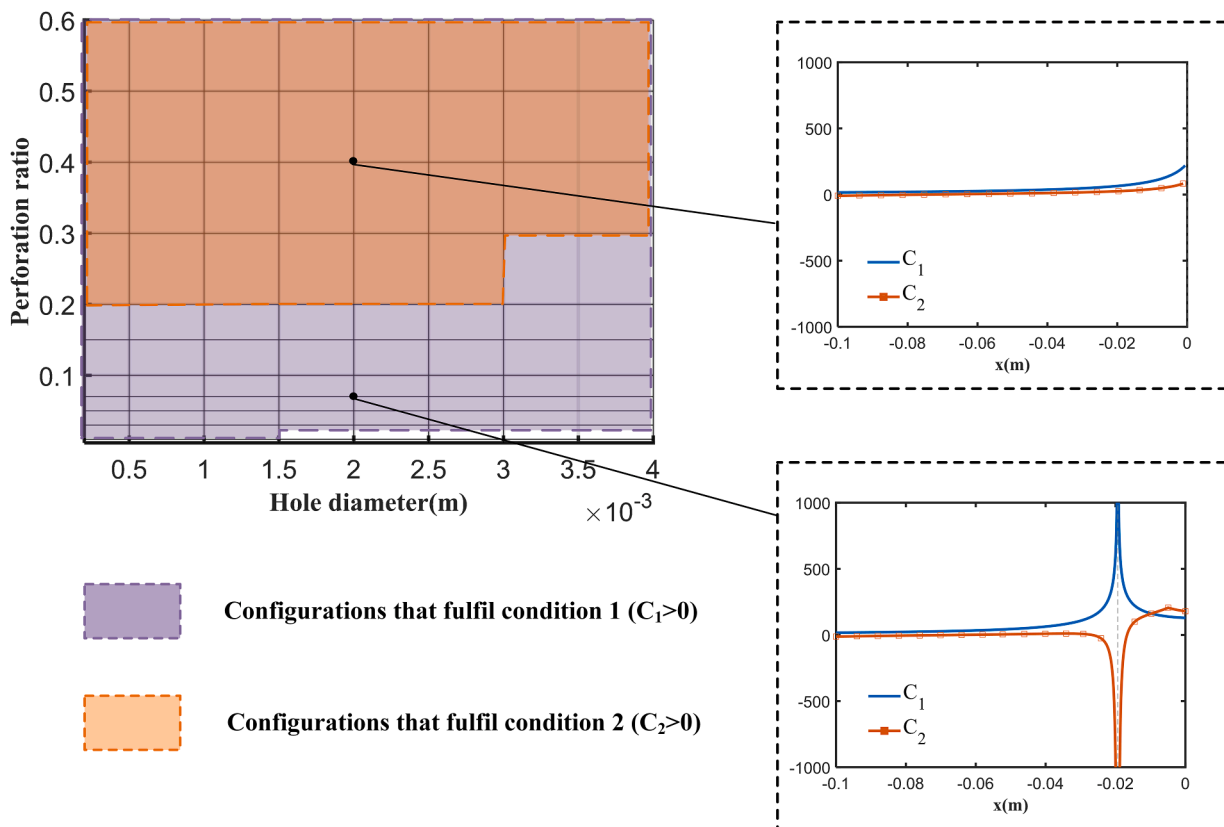


Fig. 6. Range of perforation parameters relating to the applicability of the WKB method, and the values of C_1 and C_2 in two selected cases.

4.1. Modulation mechanism of slow wave phenomenon

To achieve optimal SBH design, the influence of the perforation parameters on the slow wave effect is first explored. The perforation parameters discussed here include the perforation ratio φ and the hole diameter R_h of the PB. These two parameters together determine the number of holes in the PB. In the subsequent analyses, the thickness of the PB is not varied. Furthermore, the impact of reducing the ring number in the PMSBH on the slow wave effect is also examined to provide a reference for designing simpler PMSBH

structures in the future, while still maintaining the desired slow wave functionalities.

4.1.1. Effect of perforation ratio on slow wave phenomenon

The effect of the perforation ratio ϕ of the PB on the slow wave phenomenon is examined first. The structure of the PMSBH model used in this analysis is the same as that in Fig. 4, with detailed parameters listed in Table 2, except for the perforation ratio which is now considered as a variable. Eleven configurations with different ϕ values are selected, ranging from 0.01 to 0.6, including 0.01, 0.03, 0.05, 0.07, 0.1, 0.15, 0.2, 0.3, 0.4, 0.5, 0.6. Both the WKB method and FEM are employed to analyze the slow wave effect. Using transient FEM simulation, the elapsed time for sound waves to pass through the PMSBH section is calculated and compared across the different ϕ values. By tracing the same wave peak in the waveform at each time step, the relationship between the position and the time of the propagating sound wave in the duct can be obtained. The elapsed time can then be calculated by determining the time interval between the arrival of the wave at the entrance and its subsequent departure from the exit.

Fig. 7(a) presents the elapsed time for the incident wave to pass through the PMSBH and the variation trend with respect to increasing ϕ , from the WKB method and FEM, respectively. Since the current PMSBH structure has a fairly larger ring number of 39, the WKB solution presented in Section 2.2 can be used, as the impedance variation is rather continuous. It should be noted that for models with small ϕ , the applicability conditions for the WKB method, as discussed in Fig. 6, are not met, and therefore, there are no WKB results corresponding to this parameter range. In such cases, only FEM is used as a reference. The slight differences between the WKB and the FEM results may also arise from the presence of the reflected waves in the FEM calculations as mentioned before.

A longer propagation time within the PMSBH portion indicates more pronounced slow wave effect. From Fig. 7(a), it can be observed that the slow wave effect is prominent when ϕ reaches approximately 0.1 and persists even as ϕ continues to increase. The effect, however, is significantly weakened at a lower ϕ . Additionally, the elapsed time in the PMSBH models, normalized to the time required for sound waves to propagate freely through a duct of the same length without SBH, T/T_0 , is also calculated and shown in the right-hand side y-axis of Fig. 7(a). It follows that when ϕ is low (approaching zero), this time ratio is nearly one, suggesting the quasi-absence of the slow sound effect. When ϕ is 0.1, the time ratio is $T/T_0=3$, meaning the average sound speed across the PMSBH is reduced by three times. To further examine the variation of the wave propagating velocities in the PMSBH models, the local velocities for PMSBH with $\phi = 0.3, 0.4$ and 0.6 are calculated using the WKB method, as shown in Fig. 7(b). The results demonstrate that the slow wave effect in the structures remains persistent for these three configurations. The speed of the sound wave gradually decreases roughly following a linear trend.

The phenomenon observed in Fig. 7(a) can be explained by Fig. 8. The upper left picture of Fig. 8 displays the sound pressure distribution at a given instant from the transient simulation of a PMSBH with a ϕ of 0.01, and the bottom plot shows the admittance at the PB of this model against the admittance of the SBH with the best slow wave effect, as proposed by Mironov. Fig. 8 also illustrates the sound pressure distribution and a comparison of the admittance of the PMSBH with $\phi = 0.2$. From Fig. 8, it can be seen that when the admittance distribution of the PMSBH is closer to that of Mironov’s ideal admittance model, the slow wave effect is obviously better. When ϕ is small, there is a singularity in the admittance at a certain location of the PB. The backing cavities near this point creates a local resonance region and most of the energy of the sound wave is confined by this resonance region, thus compromising the slow wave effect. However, for a PMSBH with properly chosen parameters, the sound wave will indeed slow down alongside a compression in the wavelength, energy is gradually dissipated by the cavities and the PB as the wave propagates.

4.1.2. Effect of hole diameter on the slow wave phenomenon

The second parameter that may affect the slow-sound effect is the hole diameter of the PB, R_h . The structural parameters of the

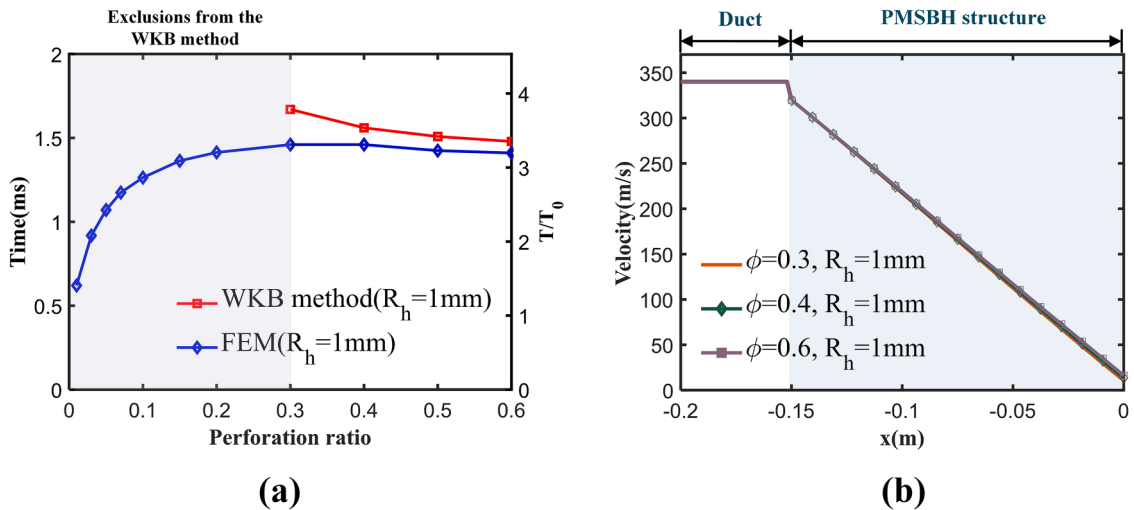


Fig. 7. (a) Elapsed time of the sound wave propagating through the PMSBH with different perforation ratios calculated by WKB method and FEM. (b) Comparison of sound velocity in the PMSBH structure with different perforation ratios by WKB method.

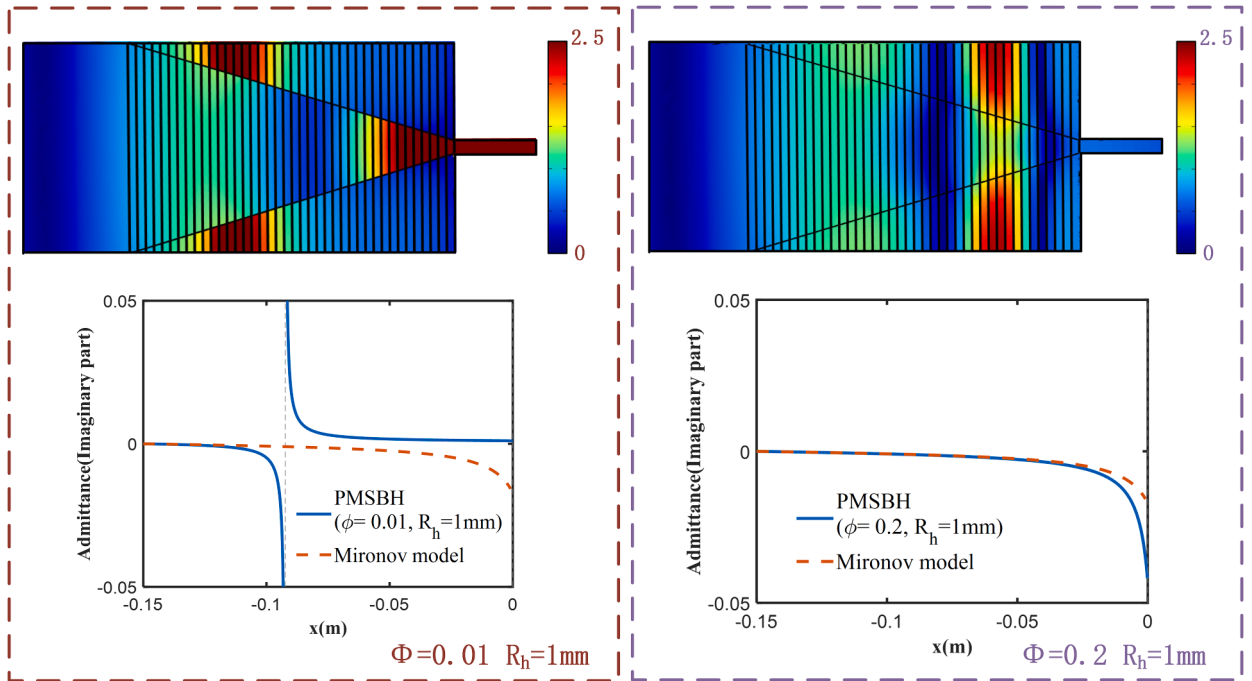


Fig. 8. Instantaneous sound pressure distributions and admittance distributions at PB in the PMSBH with a perforation ratio of 0.01 and 0.2.

PMSBH used in this section remain the same as tabulated in Table 2, except for R_h which is now considered as a variable. To investigate the effect of R_h , eight PMSBH configurations with different R_h values are selected, namely 0.2 mm, 0.5 mm, 0.8 mm, 1 mm, 1.5 mm, 2 mm, 2.5 mm and 3 mm. The perforation ratio is fixed at 0.4, within the optimal region above 0.1.

Similar to the previous section, the time taken for sound waves to propagate through each model is calculated using both the WKB method and FEM, with results presented in Fig. 9(a). The frequency of the incident wave is set to 1000 Hz. Note that for the selected parameters, all PMSBH configurations can be analyzed using the WKB solutions, as previously determined in Fig. 6. In addition, the previously defined T/T_0 is also presented in Fig. 9(a). Apart from the reflection-induced slight differences, the WKB and FEM results basically agree. More importantly, the hole diameter seems to have little effect on the slow wave phenomenon. Irrespective of the hole diameter, the PMSBH can entail a persistent slow wave effect as long as other parameters, especially the perforation ratio, are appropriately chosen.

To further understand the variation of the sound velocity in the PMSBH models, three cases with $R_h = 0.2$ mm, 1 mm and 3 mm are

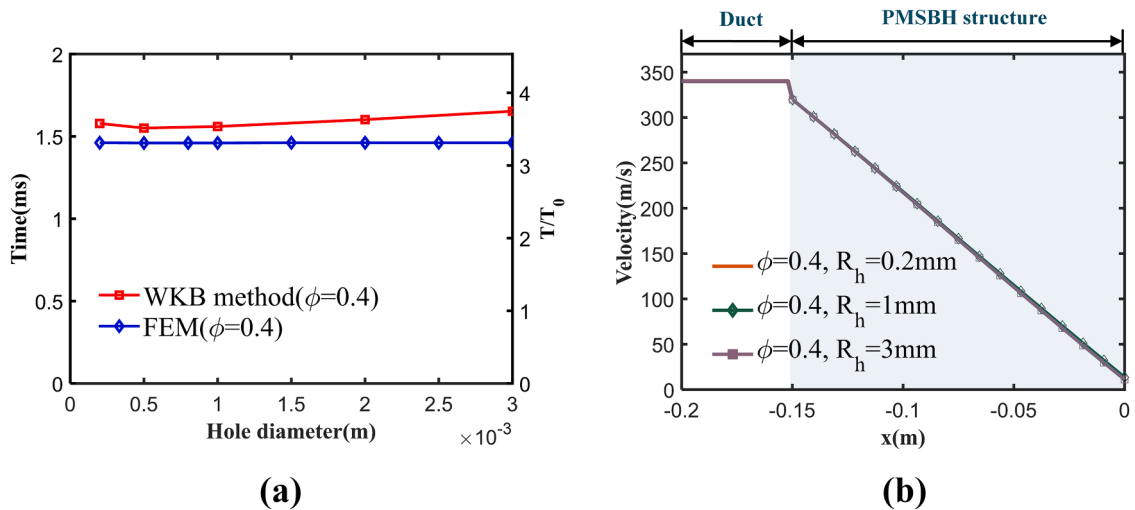


Fig. 9. (a) Elapsed time of the sound wave propagating through the PMSBH with different hole diameters calculated by WKB method and FEM. (b) Comparison of sound velocity in the PMSBH structure with different hole diameters by WKB method.

investigated, and the corresponding local velocities across the duct length are calculated by the WKB method, as shown in Fig. 9(b). A consistent effect of strong wave retarding is observed in all three configurations, which are in line with the results presented in Fig. 9 (a). Finally, Fig. 10 elucidates the underlying reasons explaining the phenomenon observed in Fig. 9(a) and (b). Once again, the admittance distribution at the PB in these PMSBHs is similar to that of the SBH proposed by Mironov for the best slow wave effect, regardless of whether the hole diameter is large or small.

4.1.3. Modulating mechanism through perforation parameter tuning

While the previous two sections analyzed the individual impact of each parameter on the slow wave effect, this section focuses on the effects of adjusting multiple parameters to achieve the best slow wave phenomenon. To ensure the parameters are varied in a sufficiently wide range, numerical results using FEM are presented, which are not constrained by the valid range, as opposed to WKB solutions. A total of 870 configurations with varying perforation ratios and hole diameters are considered. The perforation ratio ϕ ranges from 0.01 to 0.6 at an interval of 0.02, resulting in a total of 30 values that cover a wide range; the hole diameter R_h from 0.2 mm to 3 mm at an interval of 0.1 mm, resulting in a total of 29 hole diameter cases. Altogether, this yields a total of 870 data entries, which are obtained from 870 transient FEM simulations. Other parameters constituting the PMSBH structure are the same as those tabulated in Table 2.

The elapsed time for the sound wave to travel through the PMSBH section in different PMSBH structures is calculated and plotted in Fig. 11(a). From this figure, it is evident that ϕ has the greatest impact on the slow wave effect, while the effect of R_h is much less. Therefore, as long as the perforation ratio is appropriately chosen, the slow wave can always be ensured, regardless of the hole diameter. This indicates the possibility of ensuring effective slow wave performance by tuning the perforation ratio and then adjusting the hole diameter to achieve maximum acoustic energy dissipation.

Subsequently, a specific case, picked from Fig. 11(a), is selected for further analysis. By conducting time-domain simulations, the acoustic waveform on the median axis of the duct at each time instant can be obtained, as demonstrated in Fig. 11(b). By tracking the propagation position of the first wave peak, its position curve versus time can be acquired (red curve with stars). The WKB method can also be used to predict the propagation process of the sound wave in this PMSBH (red dotted curve). These results are plotted in Fig. 11 (c). Meanwhile, the figure displays the propagation position curve versus time of the first peak of the sound wave in the SBH, which has the most effective slow wave, as a reference (yellow curve with squares). Furthermore, the propagation process of the sound wave passing through a duct without PMSBH is also presented in Fig. 11(c) (blue curve). Note that the slopes of these lines represent the local velocity of the sound waves and the area between the two red dotted lines represents the PMSBH or SBH region. In the absence of SBH structure in the duct, the sound wave obviously propagates freely at a nominal sound speed of 340 m/s, as evidenced by the constant slope of the blue line. Fig. 11(c) illustrates that the slopes of the sound wave propagation curves decrease with respect to the propagation distance in both the SBH and PMSBH regions, indicating the occurrence of slow waves as evidenced by a reduction in the sound speed in both structures. Moreover, both structures have very comparable slow wave effects, suggesting that the incorporation of the PB with suitable parameters does not affect the slow wave effect of the SBH. Instead, the deployment of the PB offers the additional advantage of increasing energy dissipation.

4.1.4. Effect of ring number on the slow wave phenomenon

It has been discussed in previous research that to achieve appreciable slow wave effects in SBH design, a large number of internal rings is generally required, which is not ideal for practical applications and could pose fabrication challenges [50]. Without the inclusion of PB, reducing the number of rings can lead to a deterioration in the slow wave effect. This section further examines whether the presence of PB might facilitate the generation of the slow wave phenomenon with reduced number of rings in a PMSBH.

To answer this question, the ring number is reduced from 39 to 9, resulting in a reduction of total chamber sections from 40 to 10. Firstly, the elapsed time for the sound waves to pass through different PMSBHs is presented in Fig. 12(a). For both cases, the thickness and hole diameter of the PB, which were shown to exert less effect, are fixed as 0.4 mm and 1 mm, respectively. The perforation ratio,

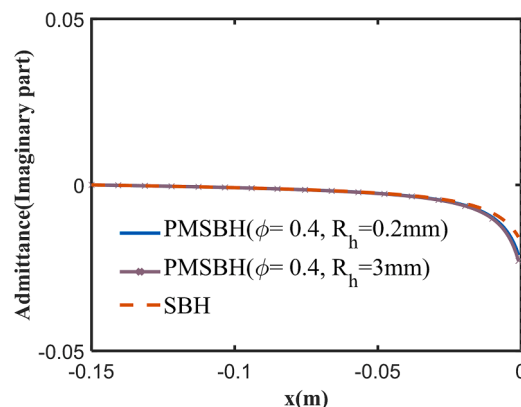


Fig. 10. Admittance distributions at PB in the PMSBH with a hole diameter of 0.2 mm and 3 mm.

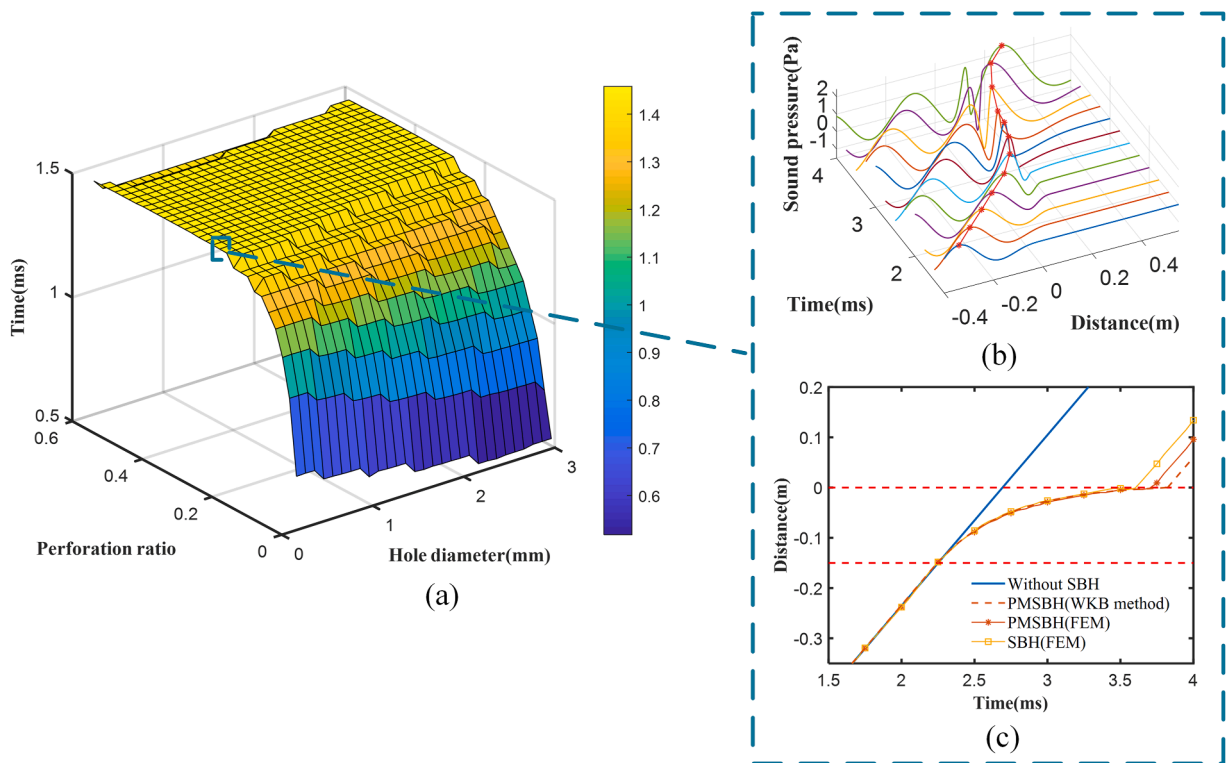


Fig. 11. (a) Elapsed time of the sound wave propagating in various PMSBH structures with different perforation ratios and hole diameters. (b) Acoustic waveform on the median axis at each time instant in the PMSBH. (c) Propagation position of the sound wave versus time in different models.

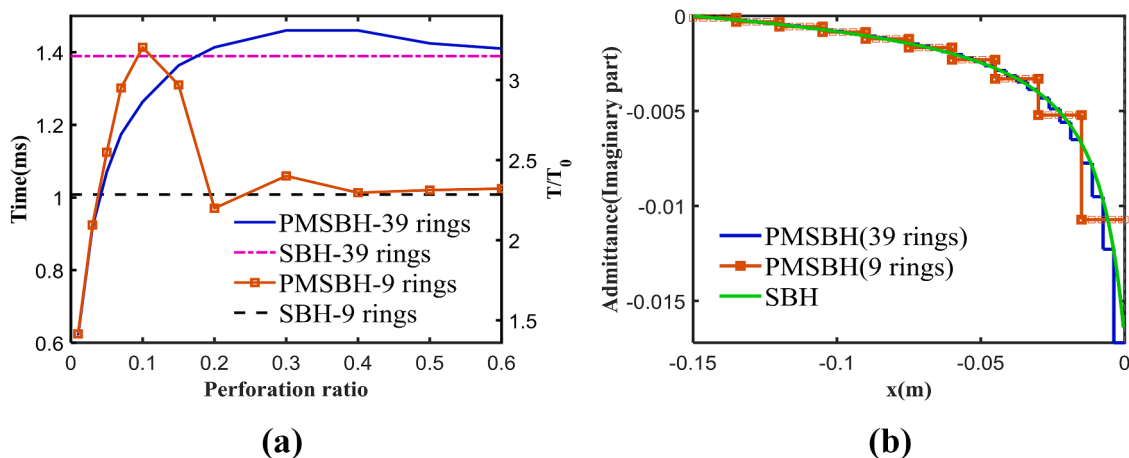


Fig. 12. (a) Elapse time for the sound waves to pass through different PMSBHs or the SBH. (b) Admittance distributions in different PMSBHs and SBH.

φ , which greatly affects the slow sound, is varied between 0.01 and 0.6. As a reference, the elapsed time for the 39-ring SBH and 9-ring SBH is also plotted in Fig. 12(a).

It can be seen from Fig. 12(a) that the 39-ring PMSBH produces strong slow-sound effect when φ is greater than 0.1, which is in agreement with the previous findings in Fig. 11(a). When the number of rings in the PMSBH is reduced to 9, the pattern of the curve drastically changes. When φ is near 0.1, the slow-sound effect of the 9-ring PMSBH is comparable to that of the 39-ring PMSBH with a large perforation ratio. However, the 9-ring SBH is unable to maintain the optimal slow wave effect as the ring number decreases. This suggests that the proposed PMSBH, by adding PB, provides the possibility of reducing the number of rings without affecting the slow-sound performance, as long as the perforation ratio is carefully selected. This can greatly simplify the design and fabrication of the

PMSBH structure.

To further explain the underlying reasons, the variations of the wall admittance along the axial direction of the 39-ring PMSBH, 9-ring PMSBH, and the ideal SBH with an infinite number of rings are presented in Fig. 12(b). The perforation ratio is set to 0.4, where the slow-sound effect in the 9-ring PMSBH has deteriorated, since this perforation ratio is not the optimal value for the 9-ring cases as shown in Fig. 12(a). The ideal SBH with an infinite number of rings shows a smooth, continuous admittance curve. In comparison, the 39-ring PMSBH model exhibits an admittance distribution that is close to the ideal SBH, which explains the better slow-sound performance observed for this configuration. In contrast, the admittance curve for the 9-ring PMSBH is discrete, and deviates significantly from the ideal SBH. This deviation likely accounts for the reduced slow-sound effect.

Note the above analyses on slow wave phenomenon were conducted for a arbitrarily chosen frequency of 1000 Hz as an illustrative example. Verifications on other frequencies are briefly discussed in Appendix A (Fig. A1(a) and (b)).

4.2. Effect of perforation parameters on the sound absorption

We now examine the impact of perforation parameters on the sound absorption performance. To achieve better sound absorption, it is essential to balance the slow wave effect with the energy dissipation effect, although the common perception is that smaller holes can enhance energy dissipation. Using the FEM model, we calculate the sound absorption coefficients for 870 cases of 9-ring PMSBHs, whose PB parameters have the same variation range as the PMSBHs previously analyzed in Fig. 11(a), except for the ring number. In addition to the dissipation provided by the small perforations, the damping loss is also introduced in the cavities behind the PB by using a complex sound speed $c_0 = 340 \times (1 + 0.03i)$ m/s. For each unique combination of the PMSBH parameters, the sound absorption coefficients from 10 to 2000 Hz (linearly sampled with 10 Hz step-size) are calculated, and the average sound absorption coefficients in this frequency range are compared in Fig. 13(a).

The results reveal that both parameters (ϕ and R_h) have significant impacts on the sound absorption performance. For the 9-ring PMSBH, Fig. 12(a) shows that the optimal slow-sound region is when ϕ lies between 0.07 and 0.15. It can be seen from the contour plot in Fig. 13(a) that the average sound absorption exhibits a narrow peak region above 0.9, which closely coincides with the optimal range for the slow sound effect, indicating the substantial advantage of harnessing this phenomenon. Interestingly, varying the hole diameter from 0.1 mm to 2 mm within the optimal ϕ range does not cause a significant deterioration of the sound absorption in the PMSBH, with an average value maintains above 0.8. This suggests that the selection of hole diameter ranges can go beyond the conventional micro-perforated panel (MPP) range, deviating from classical micro-perforation theories. Traditionally, the commonly accepted optimal parameter range for designing a MPP absorber is typically $\phi \approx 0.01$, $R_h < 0.5$ mm. In Fig. 13(a), this range corresponds to the lower-left corner, which indeed shows impressive sound absorption above 0.8. However, the lower edge of the contour shows the adverse effect of enlarging the hole diameter. When ϕ is small (close to 0.01) where the slow sound effect is absent, increasing the hole diameter results in inadequate dissipation, leading to a sharp drop in the absorption performance. At other perforation ratios above the optimal region where the slow wave effect becomes worse albeit existing, such as $\phi = 0.4$, the general trend indicates that reducing the hole size enhances energy dissipation, thereby improving sound absorption and resulting in an average sound absorption coefficient near 0.9, contrary again to traditional micro-perforation theories. These observations allow us to make effective choices in selecting perforated plate parameters while considering design trade-offs.

Among the 870 analyzed cases, the optimal result with the highest average sound absorption is identified, where the PB parameters are $\phi = 0.1$, $R_h = 0.2$ mm. Fig. 13(b) shows the sound absorption curve from 10 to 2000 Hz, in comparison with the curve for a bare 9-

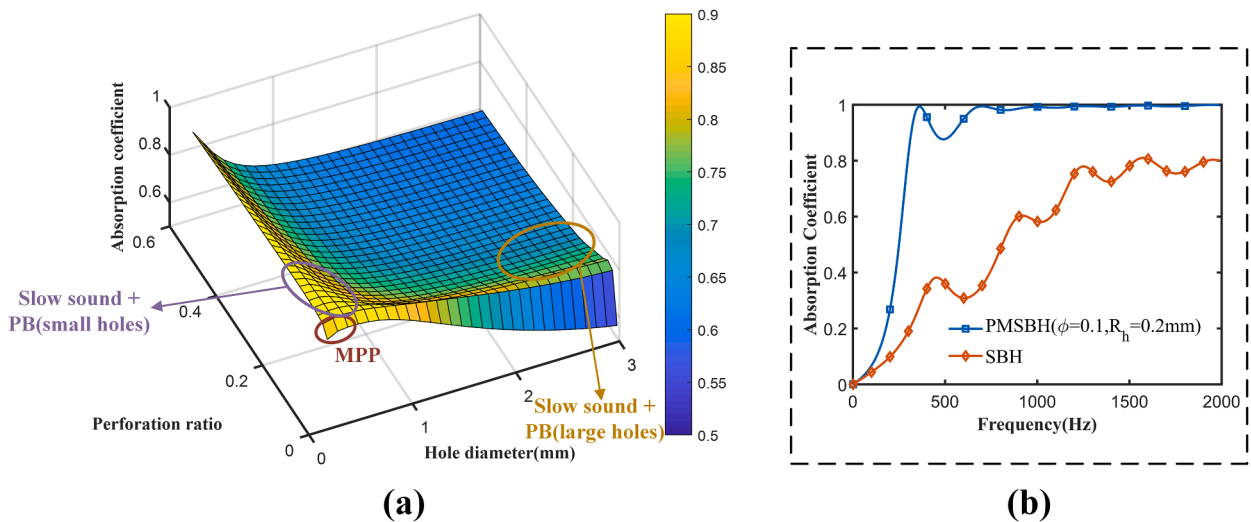


Fig. 13. (a) Contour plot showing the average sound absorption coefficient of 870 9-ring PMSBH configurations with varying perforation ratio and hole diameter. (b) Comparison of the absorption coefficients between 9-ring PMSBH and 9-ring SBH.

ring SBH without PB but with the same geometrical parameters. It is evident that the PMSBH outperforms the original SBH across the entire frequency range, exhibiting a nearly flat curve close to 1 from 500 to 2000 Hz. This demonstrates the significant advantages of incorporating PB into SBH designs. Even if the ring number is small, the performance of the 9-ring PMSBH is still outstanding over a broadband frequency range. Therefore, from a sound absorption perspective, the PMSBH offers the advantage of reducing the number of rings and simplifying the structure while maintaining its performance.

We further conclude guidelines for designing an effective slow sound absorbing device by fine-tuning the perforation parameters. To facilitate a simple and low-cost design of PMSBH, the number of rings should be kept low. Our findings suggest that a 9-ring PMSBH can provide satisfactory sound absorption, contingent upon the careful selection of PB parameters. To this end, the perforation ratio φ is identified as the primary parameter to be considered. According to Fig. 12(a), φ ranging between 0.07 and 0.15 yields the most effective slow wave propagation. By setting φ to 0.1, further adjustments to the hole diameter R_h can enhance energy dissipation. To illustrate this, Fig. 14 presents the sound absorption coefficients for PMSBHs with varying hole diameters (0.2 mm, 1 mm, 1.5 mm) while $\varphi = 0.1$. It can be seen that smaller holes exhibit higher absorption coefficients throughout the frequency range, which can be attributed to increased energy dissipation. Although the average sound absorption coefficient in the entire frequency may not differ significantly, the low-frequency performance with smaller holes is generally better. In summary, designing an efficient PMSBH absorber with fewer rings lies in the careful selection of appropriate perforation parameters. These guidelines serve as a valuable reference for the design of slow sound absorbing devices.

5. Experimental validation

The previous sections discussed the regulation mechanisms of perforation parameters based on analytical and numerical results. In this section, two experiments are conducted to verify these findings. The first time-domain experiment aims to experimentally examine the influence of perforation ratio φ on the slow wave phenomenon. The second frequency-domain experiment verifies the effect of hole diameter R_h on the sound absorption performance.

5.1. Effect of perforation ratio on the slow wave propagation

To experimentally examine the impact of the perforation ratio φ on the slow wave phenomenon, a customized acoustic duct system was constructed for conducting the experiment. Fig. 15 shows a schematic diagram of the experimental setup. This system allows for measuring the elapsed time for sound waves to reach any distance in the PMSBH in the time domain.

Three 9-ring PMSBH models with varying φ were fabricated based on the results discussed in Fig. 12(a). The SBH parts were manufactured by 3D printing using resin material. Their structural details and parameters are given in Fig. 4 and Table. 1. The perforated boundary was made using steel plates and then combined with the SBH part to form a PMSBH. The hole diameter R_h is 1 mm, and the thickness is 0.4 mm. Three 9-ring PMSBH samples were fabricated with φ selected as 0.01, 0.1 and 0.35, respectively.

As for the measurement system, a single-frequency burst signal with 5 peaks was generated from the loudspeaker at the entrance of the duct. The frequency of the burst wave was chosen to be 1000 Hz. To trace the propagation of wave packets, two MEMS microphones were installed in the system. One MEMS microphone was used as the reference, fixed at 20 cm from the tested PMSBH model upstream. The other MEMS microphone is movable, which can be positioned at various locations in the duct and within the PMSBH section. From the pressure signals recorded by the two microphones, the burst waveforms were first identified, and then the propagation time from the reference microphone to the movable microphone was determined using the correlation method. The moving range of the movable microphone is 50 cm, with a total of 22 positions in the duct chosen for measurements. These include 8 equidistant points within 20 cm from the reference microphone to the PMSBH left boundary, 10 equidistant points within the PMSBH, and 4 points in the narrow duct attached to the PMSBH termination. The movable microphone was attached to a straight carbon fiber rod with a cross-section of 4 mm in diameter.

The time of sound wave propagation from the reference microphone to each measurement position indicates the variation in sound speed. A straight line indicates a constant propagation speed, whereas a curved line with reduced slope indicates the occurrence of slow sound. The experimental results for the three different PMSBH samples are plotted in Fig. 16. Furthermore, the numerical results from FEM calculations are also presented. It can be observed that the experimental results agree well with the FEM results, which validates the previous numerical results, and vividly illustrates the slow sound phenomenon in the PMSBH structure. Comparing these results, one can observe that the slow wave effect is the strongest when φ equals to 0.1, and weakest with φ equaling to 0.01. These findings are in line with the observations from the numerical simulations. The results clearly demonstrate that the perforation ratio has a significant impact on the slow wave effect, and a suitable perforation ratio can ensure an excellent slow wave performance.

5.2. Effect of hole diameter on the sound absorption

We further experimentally verify the influence of hole diameter R_h on the sound absorption performance. As outlined in Section 4, variation in the hole size mainly affects the sound dissipation. To demonstrate this, two new PMSBH samples with identical perforation ratio ($\varphi = 0.2$) but different hole diameters (0.5 mm and 2 mm) were fabricated. By conducting the transient experiment as depicted in Section 5.1, the measured slow wave performances for the two samples, as illustrated in Fig. 17(a), show very similar behavior. The measured results again agree well with transient FEM simulations. This confirms that the hole diameter has a negligible role in slow wave propagation in the proposed PMSBH system.

Fig. 17(b) further compares the sound absorption performances for the two hole sizes. The sound absorption coefficient can be

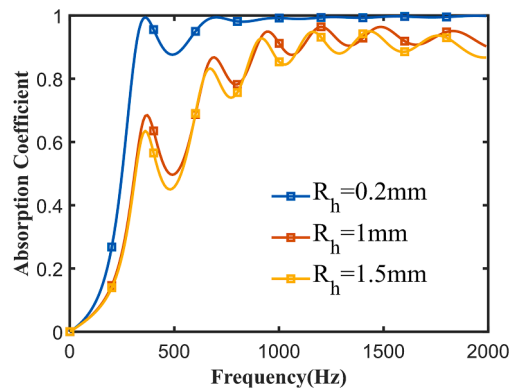


Fig. 14. Sound absorption coefficients of the 9-ring PMSBH models with different hole diameters.

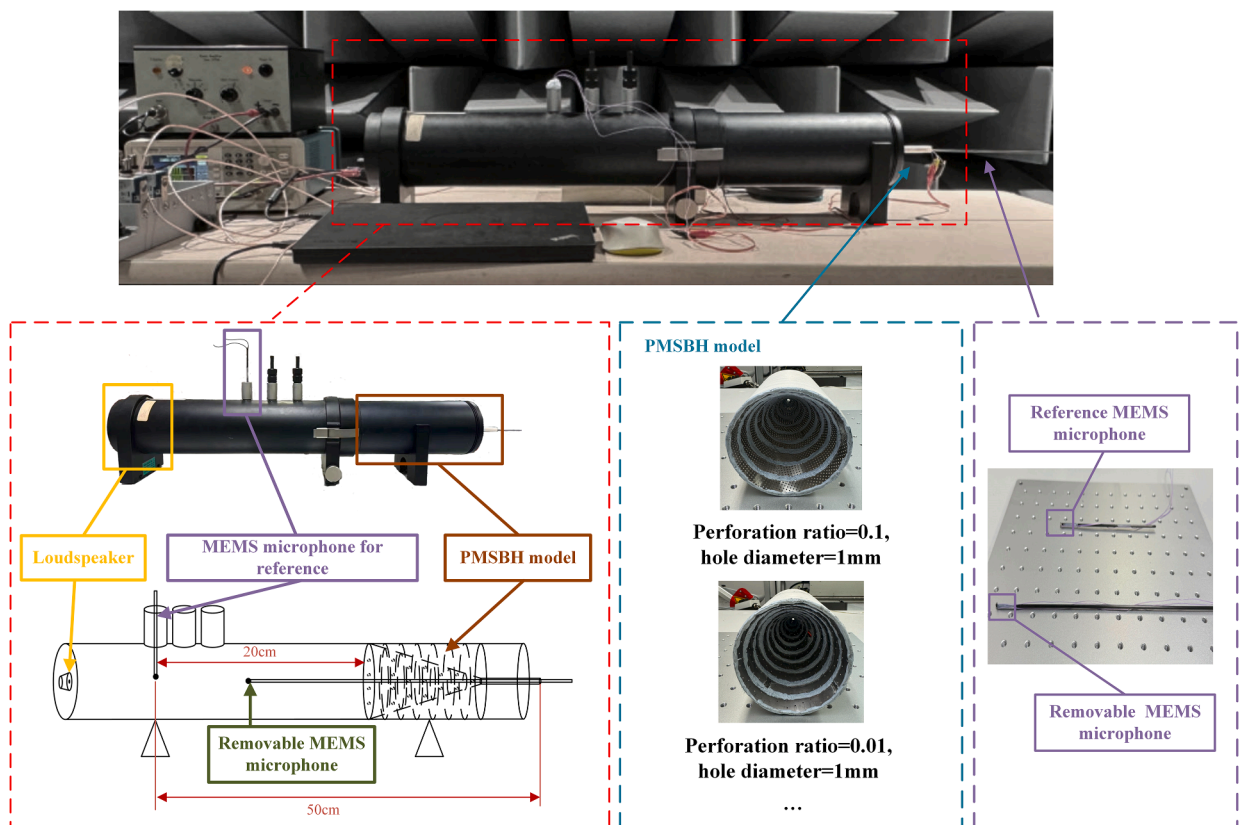


Fig. 15. Schematic diagram of the experimental set-up.

conveniently measured in a standard impedance tube, thus the detailed procedures are omitted here [33]. It can be seen that smaller hole diameter of 0.5 mm indeed performs better than the 2 mm hole, which is consistent with the trend previously observed in Fig. 14. Note the tested configurations are not the optimal ones due to the manufacturing limitations. Moreover, further reducing the hole size down to 0.2 mm was not attempted due to high fabrication costs. The result for 0.5 mm sample already shows satisfactory broadband performance. These experimental insights confirm the major conclusions from the preceding mechanism analyses, and underscore the importance of selecting appropriate perforation parameters to enhance the sound absorption efficiency of PMSBH.

6. Conclusions

In this work, a perforation-modulated SBH (PMSBH) retarding structure is investigated, which introduces tunability into the SBH design. By adjusting the perforation parameters, two crucial physical phenomena in the PMSBH, namely the slow wave effect and

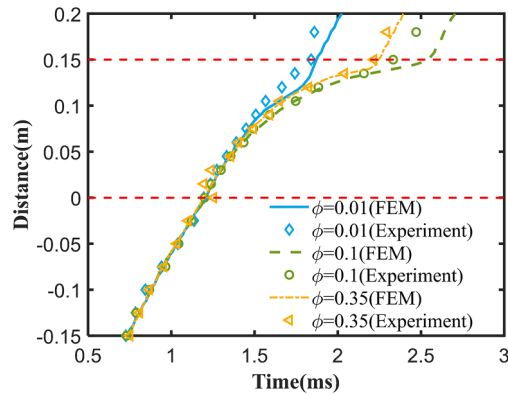


Fig. 16. Propagation distance curves of sound wave versus time in PMSBH models with different perforation ratios.

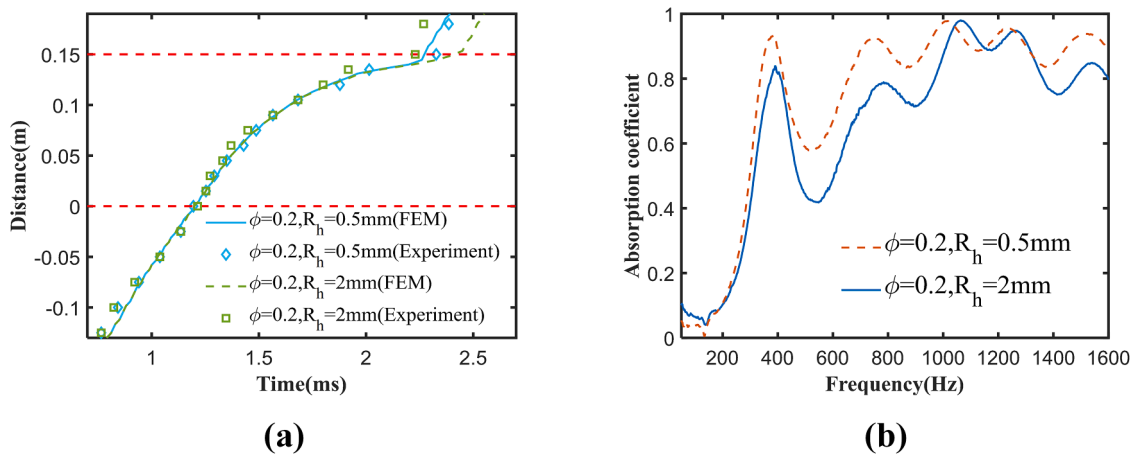


Fig. 17. (a) Propagation distance curves of sound wave versus time in PMSBH models with different hole diameters. (b) Sound absorption of PMSBH models with different hole diameters.

energy dissipation, can be balanced to eventually enhance the overall sound absorption performance. Two sets of WKB solutions are developed for predicting the sound wave propagation in the PMSBH structures with continuous and discrete admittance variations, respectively. The range of applicability for these WKB solutions are also examined using analytical method and numerical methods. The validity of the WKB solutions is verified through comparisons with Mironov's ideal model and FEM results.

The influence of the perforation ratio and the hole diameter on the slow wave effect is investigated using the established WKB solutions and the FEM results, with experimental confirmation in a later section. The perforation ratio is shown to have a much greater impact on the slow wave phenomenon than the hole diameter. An appropriate perforation ratio can reliably ensure significant slow sound phenomenon, even at a reduced ring number. Furthermore, the effects of these two parameters on the sound absorption performance are also explored. Both parameters affect sound absorption. Depending on the ring numbers, the optimal range for the perforation ratio and the hole size go beyond the typical range widely adopted in the MPP community when the slow wave effect is absent. While the former ensures effective slow wave effects, the latter adds effective energy dissipation to the process, both combined together yielding superior sound absorption. In summary, the modulation mechanisms through tuning the perforation parameters in the PMSBH provide a new perspective to the existing SBH design and offer a guideline to design a PMSBH with reduced ring number and simplified structural configuration which are able to simultaneously achieve effective slow wave effect and excellent sound absorption performance.

CRedit authorship contribution statement

Sihui Li: Writing – original draft, Visualization, Validation, Software, Methodology, Investigation, Data curation. **Xiang Yu:** Writing – review & editing, Supervision, Software, Project administration, Methodology, Formal analysis. **Li Cheng:** Writing – review & editing, Supervision, Resources, Project administration, Methodology, Funding acquisition, Conceptualization.

Declaration of competing interest

The authors declare that they have no known competing financial interests or personal relationships that could have appeared to influence the work reported in this paper.

Acknowledgments

This research is supported by Research Grants Council of Hong Kong under Grant No. PolyU 15201822. Yu Xiang acknowledges the start-up funding support from the Department of Mechanical Engineering and the Hong Kong Polytechnic University.

Appendix A. Slow waves at other frequencies

The previous calculations and analyses are only discussed in relation to the case of acoustic frequencies at 1000 Hz. It needs clarification whether the slow wave phenomenon still exists in the PMSBH at other frequencies and whether the slow wave effect remains consistent at different frequencies. The WKB method is employed to explore these questions. Firstly, the local wave number in a PMSBH at different frequencies (800 Hz, 1000 Hz, 1500 Hz, 2000 Hz) is obtained and plotted in Fig. A1(a). Except for its perforation ratio of 0.4 and the hole diameter of 1 mm, other parameters of this PMSBH model are tabulated in Table 2. The cut-off frequency is 2074 Hz. The PMSBH is placed between -0.15 m and 0 m, corresponding to the inlet and outlet ends, respectively. It is clear that at different frequencies, the wave number of the sound wave gradually increases as it enters the PMSBH structures, which implies that the velocities gradually decrease in the PMSBH and the presence of the slow wave. Further, the velocity variations of the sound wave of different frequencies in the same PMSBH are exhibited in Fig. A1(b). The velocity curves at different frequencies are in agreement, suggesting that the structure has a comparable slow wave effect on these sound waves at different frequencies. Thus, the previous conclusions remain valid over a wide frequency range.

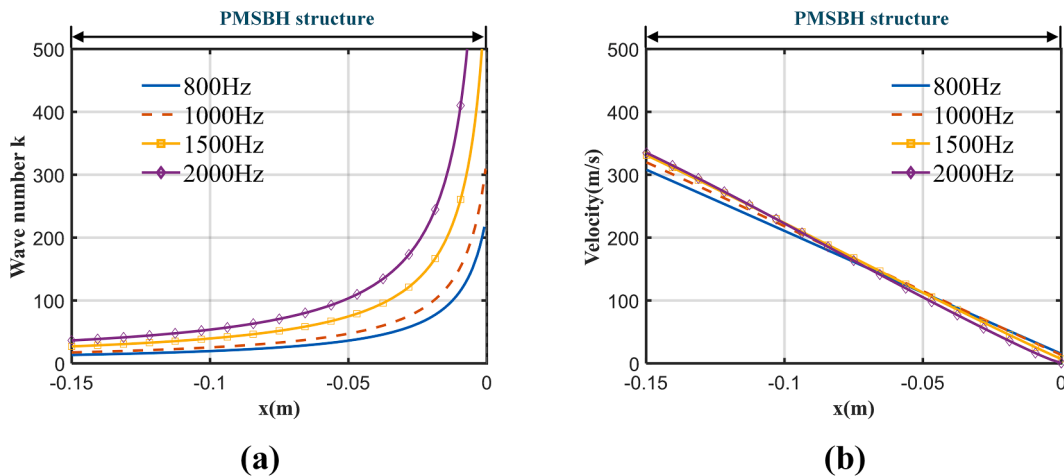


Fig. A.1. (a) Local wave number in the PMSBH at different frequencies. (b) Velocity variations of the sound wave in the PMSBH at different frequencies.

Data availability

Data will be made available on request.

References

- [1] J. Deng, O. Guasch, L. Zheng, A semi-analytical method for characterizing vibrations in circular beams with embedded acoustic black holes, *J. Sound Vib.* 476 (2020) 115307, <https://doi.org/10.1016/j.jsv.2020.115307>.
- [2] D.J. O'Boy, V.V. Krylov, V. Kralovic, Damping of flexural vibrations in rectangular plates using the acoustic black hole effect, *J. Sound Vib.* 329 (2010) 4672–4688, <https://doi.org/10.1016/j.jsv.2010.05.019>.
- [3] L. Tang, L. Cheng, H. Ji, J. Qiu, Characterization of acoustic black hole effect using a one-dimensional fully-coupled and wavelet-decomposed semi-analytical model, *J. Sound Vib.* 374 (2016) 172–184, <https://doi.org/10.1016/j.jsv.2016.03.031>.
- [4] J. Deng, L. Zheng, P. Zeng, Y. Zuo, O. Guasch, Passive constrained viscoelastic layers to improve the efficiency of truncated acoustic black holes in beams, *Mech. Syst. Signal Process.* 118 (2019) 461–476, <https://doi.org/10.1016/j.ymsp.2018.08.053>.
- [5] L. Ma, L. Cheng, Numerical and experimental benchmark solutions on vibration and sound radiation of an Acoustic Black Hole plate, *Appl. Acoust.* 163 (2020) 107223, <https://doi.org/10.1016/j.apacoust.2020.107223>.

- [6] J. Deng, O. Guasch, L. Maxit, L. Zheng, Annular acoustic black holes to reduce sound radiation from cylindrical shells, *Mech. Syst. Signal Process.* 158 (2021) 107722, <https://doi.org/10.1016/j.ymssp.2021.107722>.
- [7] J.Y. Lee, W. Jeon, Wave-based analysis of the cut-on frequency of curved acoustic black holes, *J. Sound Vib.* 492 (2021) 115731, <https://doi.org/10.1016/j.jsv.2020.115731>.
- [8] V.V. Krylov, F.J.B.S. Tilman, Acoustic 'black holes' for flexural waves as effective vibration dampers, *J. Sound Vib.* 274 (2004) 605–619, <https://doi.org/10.1016/j.jsv.2003.05.010>.
- [9] J. Deng, N. Gao, X. Chen, B. Han, H. Ji, Evanescent waves in a metabeam attached with lossy acoustic black hole pillars, *Mech. Syst. Signal Process.* 191 (2023) 110182, <https://doi.org/10.1016/j.ymssp.2023.110182>.
- [10] L. Tang, L. Cheng, Impaired sound radiation in plates with periodic tunneled Acoustic Black Holes, *Mech. Syst. Signal Process.* 135 (2020) 106410, <https://doi.org/10.1016/j.ymssp.2019.106410>.
- [11] C.A. McCormick, M.R. Shepherd, Design optimization and performance comparison of three styles of one-dimensional acoustic black hole vibration absorbers, *J. Sound Vib.* 470 (2020) 115164, <https://doi.org/10.1016/j.jsv.2019.115164>.
- [12] J. Deng, O. Guasch, L. Maxit, L. Zheng, Transmission loss of plates with multiple embedded acoustic black holes using statistical modal energy distribution analysis, *Mech. Syst. Signal Process.* 150 (2021) 107262, <https://doi.org/10.1016/j.ymssp.2020.107262>.
- [13] T. Zhou, L. Cheng, Planar swirl-shaped acoustic black hole absorbers for multi-directional vibration suppression, *J. Sound Vib.* 516 (2022) 116500, <https://doi.org/10.1016/j.jsv.2021.116500>.
- [14] J. Deng, O. Guasch, L. Maxit, L. Zheng, Vibration of cylindrical shells with embedded annular acoustic black holes using the Rayleigh-Ritz method with Gaussian basis functions, *Mech. Syst. Signal Process.* 150 (2021) 107225, <https://doi.org/10.1016/j.ymssp.2020.107225>.
- [15] J. Deng, O. Guasch, L. Zheng, T. Song, Y. Cao, Semi-analytical model of an acoustic black hole piezoelectric bimorph cantilever for energy harvesting, *J. Sound Vib.* 494 (2021) 115790, <https://doi.org/10.1016/j.jsv.2020.115790>.
- [16] J. Deng, Y. Xu, O. Guasch, N. Gao, L. Tang, X. Chen, A two-dimensional wave and Rayleigh-Ritz method for complex dispersion in periodic arrays of circular damped acoustic black holes, *Mech. Syst. Signal Process.* 200 (2023) 110507, <https://doi.org/10.1016/j.ymssp.2023.110507>.
- [17] W. Huang, H. Ji, J. Qiu, L. Cheng, Wave energy focalization in a plate with imperfect two-dimensional acoustic black hole indentation, *J. Vib. Acoust.* 138 (2016) 061004, <https://doi.org/10.1115/1.4034080>.
- [18] L. Zhao, F. Semperlotti, Embedded Acoustic Black Holes for semi-passive broadband vibration attenuation in thin-walled structures, *J. Sound Vib.* 388 (2017) 42–52, <https://doi.org/10.1016/j.jsv.2016.10.029>.
- [19] J. Deng, L. Zheng, O. Guasch, H. Wu, P. Zeng, Y. Zuo, Gaussian expansion for the vibration analysis of plates with multiple acoustic black holes indentations, *Mech. Syst. Signal Process.* 131 (2019) 317–334, <https://doi.org/10.1016/j.ymssp.2019.05.024>.
- [20] H. Ji, X. Wang, J. Qiu, L. Cheng, Y. Wu, C. Zhang, Noise reduction inside a cavity coupled to a flexible plate with embedded 2-D acoustic black holes, *J. Sound Vib.* 455 (2019) 324–338, <https://doi.org/10.1016/j.jsv.2019.05.004>.
- [21] J. Deng, Y. Xu, O. Guasch, N. Gao, L. Tang, W. Guo, A wave and Rayleigh-Ritz method to compute complex dispersion curves in periodic lossy acoustic black holes, *J. Sound Vib.* 546 (2023) 117449, <https://doi.org/10.1016/j.jsv.2022.117449>.
- [22] L. Tang, L. Cheng, Broadband locally resonant band gaps in periodic beam structures with embedded acoustic black holes, *J. Appl. Phys.* 121 (2017) 194901, <https://doi.org/10.1063/1.4983459>.
- [23] L. Tang, L. Cheng, Ultrawide band gaps in beams with double-leaf acoustic black hole indentations, *J. Acoust. Soc. Am.* 142 (2017) 2802, <https://doi.org/10.1121/1.5009582>.
- [24] N. Gao, B. Wang, K. Lu, H. Hou, Complex band structure and evanescent Bloch wave propagation of periodic nested acoustic black hole phononic structure, *Appl. Acoust.* 177 (2021) 107906, <https://doi.org/10.1016/j.apacoust.2020.107906>.
- [25] W. Gao, Z. Qin, F. Chu, Broadband vibration suppression of rainbow metamaterials with acoustic black hole, *Int. J. Mech. Sci.* 228 (2022) 107485, <https://doi.org/10.1016/j.ijmecsci.2022.107485>.
- [26] A. Mousavi, M. Berggren, E. Wadbro, How the waveguide acoustic black hole works: a study of possible damping mechanisms, *J. Acoust. Soc. Am.* 151 (2022) 4279, <https://doi.org/10.1121/10.0011788>.
- [27] X. Liang, H. Liang, J. Chu, W. Wang, N. Li, Z. Yang, G. Zhou, N. Gao, C. Hu, Z. Zhou, A modified sonic black hole structure for improving and broadening sound absorption, *Appl. Acoust.* 210 (2023) 109440, <https://doi.org/10.1016/j.apacoust.2023.109440>.
- [28] O. Umnova, D. Brooke, P. Leclaire, T. Dupont, Multiple resonances in lossy acoustic black holes - theory and experiment, *J. Sound Vib.* 543 (2023) 117377, <https://doi.org/10.1016/j.jsv.2022.117377>.
- [29] Y. Chen, K. Yu, Q. Fu, J. Zhang, X. Lu, X. Du, X. Sun, A broadband and low-frequency sound absorber of sonic black holes with multi-layered micro-perforated panels, *Appl. Acoust.* 217 (2024) 109817, <https://doi.org/10.1016/j.apacoust.2023.109817>.
- [30] M.A. Mironov, V.V. Pisyakov, One-dimensional acoustic waves in retarding structures with propagation velocity tending to zero, *Acoust. Phys.* 48 (2002) 347–352, <https://doi.org/10.1134/1.1478121>.
- [31] O. Guasch, P. Sánchez-Martín, D. Ghilardi, Application of the transfer matrix approximation for wave propagation in a metafluid representing an acoustic black hole duct termination, *Appl. Math. Model.* 77 (2020) 1881–1893, <https://doi.org/10.1016/j.apm.2019.09.039>.
- [32] Y. Mi, W. Zhai, L. Cheng, C. Xi, X. Yu, Wave trapping by acoustic black hole: simultaneous reduction of sound reflection and transmission, *Appl. Phys. Lett.* 118 (2021) 114101, <https://doi.org/10.1063/5.0042514>.
- [33] X. Zhang, L. Cheng, Broadband and low frequency sound absorption by Sonic black holes with Micro-perforated boundaries, *J. Sound Vib.* 512 (2021) 116401, <https://doi.org/10.1016/j.jsv.2021.116401>.
- [34] J. Deng, O. Guasch, D. Ghilardi, Solution and analysis of a continuum model of sonic black hole for duct terminations, *Appl. Math. Model.* 129 (2024) 191–206, <https://doi.org/10.1016/j.apm.2024.01.046>.
- [35] M. Cervenka, M. Bednařík, On the role of resonance and thermoviscous losses in an implementation of “acoustic black hole” for sound absorption in air, *Wave Motion* 114 (2022) 103039, <https://doi.org/10.1016/j.wavemoti.2022.103039>.
- [36] Y. Mi, L. Cheng, W. Zhai, X. Yu, Broadband low-frequency sound attenuation in duct with embedded periodic sonic black holes, *J. Sound Vib.* 536 (2022) 117138, <https://doi.org/10.1016/j.jsv.2022.117138>.
- [37] G. Serra, O. Guasch, M. Arnela, D. Miralles, Optimization of the profile and distribution of absorption material in sonic black holes, *Mech. Syst. Signal Process.* 202 (2023) 110707, <https://doi.org/10.1016/j.ymssp.2023.110707>.
- [38] M. Cervenka, M. Bednařík, Optimal shaping of acoustic black holes for sound absorption in air, *Acta Acust.* 8 (2024) 21, <https://doi.org/10.1051/aacus/2024014>.
- [39] V. Hruška, J.P. Groby, M. Bednařík, Complex frequency analysis and source of losses in rectangular sonic black holes, *J. Sound Vib.* 571 (2024) 118107, <https://doi.org/10.1016/j.jsv.2023.118107>.
- [40] N. Sharma, O. Umnova, A. Moorhouse, Low frequency sound absorption through a muffler with metamaterial lining, in: *Proceedings of the International Congress on Sound and Vibration, London, 2017, 23-27 July 2017*.
- [41] T. Bravo, C. Maury, Broadband sound attenuation and absorption by duct silencers based on the acoustic black hole effect: Simulations and experiments, *J. Sound Vib.* 561 (2023) 117825, <https://doi.org/10.1016/j.jsv.2023.117825>.
- [42] J.W. Chua, X. Li, X. Yu, W. Zhai, Novel slow-sound lattice absorbers based on the sonic black hole, *Compos. Struct.* 304 (2023) 116434, <https://doi.org/10.1016/j.compstruct.2022.116434>.
- [43] J. Deng, O. Guasch, Sound waves in continuum models of periodic sonic black holes, *Mech. Syst. Signal Process.* 205 (2023) 110853, <https://doi.org/10.1016/j.ymssp.2023.110853>.
- [44] M. Bednařík, M. Cervenka, A sonic black hole of a rectangular cross-section, *Appl. Math. Model.* 125 (2024) 529–543, <https://doi.org/10.1016/j.apm.2023.09.005>.

- [45] M. Červenka, M. Bednařík, Numerical study of the behavior of rectangular acoustic black holes for sound absorption in air, *Wave Motion* 123 (2023) 103230, <https://doi.org/10.1016/j.wavemoti.2023.103230>.
- [46] M. Mironov, V. Pisylyakov, One-dimensional sonic black holes: Exact analytical solution and experiments, *J. Sound Vib.* 473 (2020) 115223, <https://doi.org/10.1016/j.jsv.2020.115223>.
- [47] L. Peng, Q. Mao, H. Wang, L. Lai, Q. Shi, M. Chen, Enhanced sound absorption with the combined sonic black holes, *Appl. Acoust.* 219 (2024) 109932, <https://doi.org/10.1016/j.apacoust.2024.109932>.
- [48] H. Sheng, M.X. He, H.P. Lee, Q. Ding, Quasi-periodic sonic black hole with low-frequency acoustic and elastic bandgaps, *Compos. Struct.* 337 (2024) 118046, <https://doi.org/10.1016/j.compstruct.2024.118046>.
- [49] X. Zhang, N. He, L. Cheng, X. Yu, L. Zhang, F. Hu, Sound absorption in sonic black holes: wave retarding effect with broadband cavity resonance, *Appl. Acoust.* 221 (2024) 110007, <https://doi.org/10.1016/j.apacoust.2024.110007>.
- [50] S. Li, J. Xia, X. Yu, X. Zhang, L. Cheng, A sonic black hole structure with perforated boundary for slow wave generation, *J. Sound Vib.* 559 (2023) 117781, <https://doi.org/10.1016/j.jsv.2023.117781>.